Article:
Zhang, W., Li, Guang-Jin, Ren, B. et al. (2023) Demagnetization analysis of modular SPM machine based on coupled electromagnetic-thermal modelling. Energies, 16 (1). 131. ISSN: 1996-1073

https://doi.org/10.3390/en16010131

energies

MDPI

Article

Demagnetization Analysis of Modular SPM Machine Based on Coupled Electromagnetic-Thermal Modelling

Wei Zhang [1], Guang-Jin Li [1,*], Zi-Qiang Zhu [1], Bo Ren [2], Yew Chuan Chong [2] and Melanie Michon [2]

[1] Electrical Machines & Drives Group, Department of Electronic and Electrical Engineering, University of Sheffield, Sheffield S10 2TN, UK
[2] Motor Design Limited, Wrexham LL13 7YT, UK
* Correspondence: g.li@sheffield.ac.uk

Abstract: This paper investigates magnet demagnetization characteristics of the modular permanent magnet machine. The influence of flux gaps on magnet flux density, losses distribution, torque and demagnetization are analyzed for different operating conditions. The magnet demagnetizations caused by three sources, such as the PM field, the armature field, and the magnet temperature rise, are individually investigated using the frozen permeability method. Furthermore, coupled electromagnetic (EM)-thermal modelling is also adopted in this paper to fully reveal the advantages of the modular machine in improving machine EM performances. This is essential due to the temperature-dependent properties of the machines, such as the magnet remanence, coercivity, and copper resistivity. For comparison propose, the EM performances with a particular focus on the demagnetization withstand capability for both the modular and non-modular machines are investigated based on the EM-thermal coupling. It is found that, compared to the non-modular machine, the modular machine can achieve higher torque, higher efficiency, and better demagnetization withstand capability.

Keywords: coupled electromagnetic-thermal modelling; flux gaps; frozen permeability; irreversible demagnetization; modular SPM machine

Citation: Zhang, W.; Li, G.-J.; Zhu, Z.-Q.; Ren, B.; Chong, Y.C.; Michon, M. Demagnetization Analysis of Modular SPM Machine Based on Coupled Electromagnetic-Thermal Modelling. *Energies* **2023**, *16*, 131. https://doi.org/10.3390/en16010131

Academic Editor: Massimo Panella

Received: 30 November 2022
Revised: 13 December 2022
Accepted: 21 December 2022
Published: 23 December 2022

1. Introduction

Permanent magnet (PM) machines are attracting increasing interest in various industry sectors, such as electric and hybrid electric vehicles, renewable energy, and aerospace applications. Compared with induction machines and variable reluctance machines, the PM machines have higher torque or power density and efficiency. In recent years, a novel class of PM machines with segmented stators, as shown in Figure 1a, have been proposed [1,2]. Such modular PM machines do not only have the advantages of conventional PM machines but can also simplify the manufacturing and transportation of large-scale machines. This makes them a promising candidate for direct-drive wind power applications. In addition, if the slot and pole number combination and the flux gap (FG) width are properly selected, the modular machine can also achieve improved back-EMF and average torque as well as reduced machine total mass [3]. This is mainly because the FGs in alternate stator teeth improve the winding factor (more precisely, pitch factor) and open-circuit airgap flux density and they also have a flux focusing effect. It is worth noting that, these threefold effects are true for the modular machines with a pole number (2p) larger than the slot number (Ns). By contrast, for the modular machines with 2p < Ns, the introduced flux gaps will reduce the winding factor and also have a flux defocusing effect, which leads to reduced average torque [4].

However, as for all other PM machines, the modular PM machines also face problems, such as magnet irreversible demagnetization, i.e., the magnet working point moves to below the knee point on the B(H) curve. Once irreversible demagnetization occurs, the magnet remanence permanently reduces, which leads to reduced torque or power density.

This is particularly problematic for machines operating at high temperature, which require flux weakening to achieve a wide constant power speed range. Therefore, it is essential to improve the machine demagnetization withstand capability. According to [5], it is found that for a given operating temperature, the demagnetization withstand capability of the modular machine is better than that of the conventional PM machine.

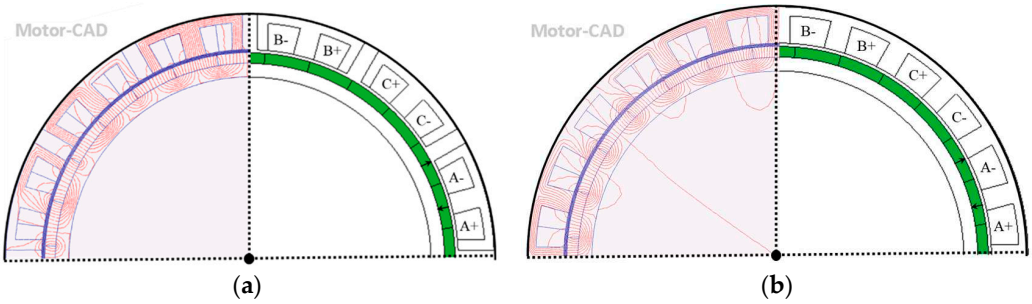

(**a**) (**b**)

Figure 1. Cross-sections and open-circuit flux line distribution of SPM machines. (**a**) Modular machine and (**b**) non-modular machine.

In the literature, some existing research works have investigated the demagnetization characteristics of PM machines. It has been found that both machine topologies, load current and magnet temperature can affect the demagnetization withstand capability of PM machines. For example, the modular SPM machines [5] and the switched flux hybrid magnet memory machine with E-core structure and PMs being inserted into the iron bridge [6] can help improve the magnet demagnetization withstand capability and significantly reduce the demagnetization area. It is also found that the area near the center line of the magnet often suffers from the most significant demagnetization for the modular SPM machine [5] and V-shaped IPM machine [7]. However, the two ends of the magnets suffer from the most significant demagnetization for the 2-layer UV-shaped IPM machine [8] and switched flux PM machine [9,10]. Apart from the machine topologies, the load current (both d- and q-axis currents) and magnet temperature can affect the demagnetization characteristics, such as flux density distribution, demagnetization ratio, electromagnetic (EM) torque and losses (e.g., PM eddy current loss, and stator and rotor core iron losses) [5,11,12].

However, most of the investigations are based on electromagnetic (EM) simulations only. Although the operating temperatures are often given for different operating conditions, the coupling between electromagnetic and thermal performances are largely neglected. Such models only consider the impact of temperature variation on machine electromagnetic performance but fail to consider the impact of electromagnetic performance variation on machine thermal performance. It is well-known that the materials' properties, such as the magnet remanence, coercivity and copper resistivity, are temperature-dependent [12,13]. Different operating temperatures can lead to the variations in machine demagnetization characteristics as well as losses, including PM eddy current loss, stator and rotor iron core losses and copper loss. These losses are the main heat sources, and their variations will, in turn, affect the temperature distribution within electrical machines. Therefore, a closely coupled EM-thermal modelling, as depicted by the flowchart in Figure 2, is essential to accurately analyze the EM's performance, such as magnet demagnetization, and the thermal performance, such as temperature distribution within different machine components at different operation conditions [14,15]. The mechanism of coupled EM-thermal modelling can be explained as follows. The machine specifications and the initial operating temperature are firstly used for calculating the initial EM performance, in particular the stator and rotor iron core losses, the PM eddy current loss and copper loss. These losses are then adopted as the input in the 3D lumped parameter thermal model (LPTN) for predicting temperature distribution within machine components. The resultant temperature can be used for updating the magnet properties, e.g., remanence and coercivity, and coil resistance, which can be used in the EM model to obtain updated EM performance.

Several iterations will be needed to solve the coupled EM-thermal model. The criterion to decide when to stop the iteration is when the temperature difference (ΔT) is lower than the convergence error (ε_{error}), then the obtained temperature distribution and EM performance can be regarded as the final predictions.

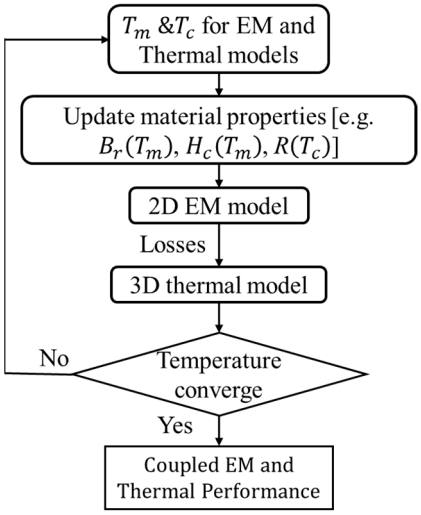

Figure 2. The flowchart of the coupled EM-thermal modelling. T_m, T_c, B_r, H_c, and R are the magnet temperature, the coil temperature, the magnet remanence, the magnet coercivity, and the coil resistance, respectively.

In this paper, a modular machine investigated in [3] (the specifications are listed in Table 1) is compared with the conventional non-modular machine, as shown in Figure 1b. Their masses of active materials and other key EM performances, i.e., maximum torque, rated power, and efficiency are compared, as listed in Table 2. The dynamic performances at room temperature for both investigated machines are compared, as shown in Figures 3 and 4. They reveal that the modular machine can achieve higher torque density and low PM loss under most operation conditions. Hence, even the iron losses of the modular machine are higher than the non-modular machine, its efficiencies under most operation conditions are higher.

The demagnetization characteristics of both the modular and non-modular machines will also be studied in this paper. They can reveal the potential of the modular machine in improving the machine demagnetization withstand capability. In addition, the machine EM performances, including PM eddy current loss, stator and rotor iron losses and torque, are significantly affected by the demagnetization. This will also be investigated based on the coupled EM-thermal modelling.

Table 1. General parameters of the investigated SPM machines.

Slot number	24	Rotor outer radius (mm)	129.4
Pole number	28	Rotor yoke thickness (mm)	8.6
Stator outer radius (mm)	154	Stack length (mm)	210
Stator yoke height (mm)	5.6	DC voltage (V)	800
Tooth width (mm)	13.2	Rated phase current (A_{peak})	100
Flux gap width (mm)	10	Number of turns per coil	10
Airgap length (mm)	2	Rate speed (rpm)	1500
Magnet thickness (mm)	6.6		

Table 2. Masses of active materials and key EM performance comparisons between the modular and non-modular SPM machine.

	Non-Modular Machine	Modular Machine
Mass of active winding (kg)	9.1	7.1
Mass of stator steel (kg)	16.7	15.7
Mass of rotor steel (kg)	10	10
Mass of permanent (kg)	8.2	8.2
Slot fill factor	0.6	0.47
Torque (Nm)	273	330
Power (kW)	43	52
Efficiency (%)	96.9	96.8

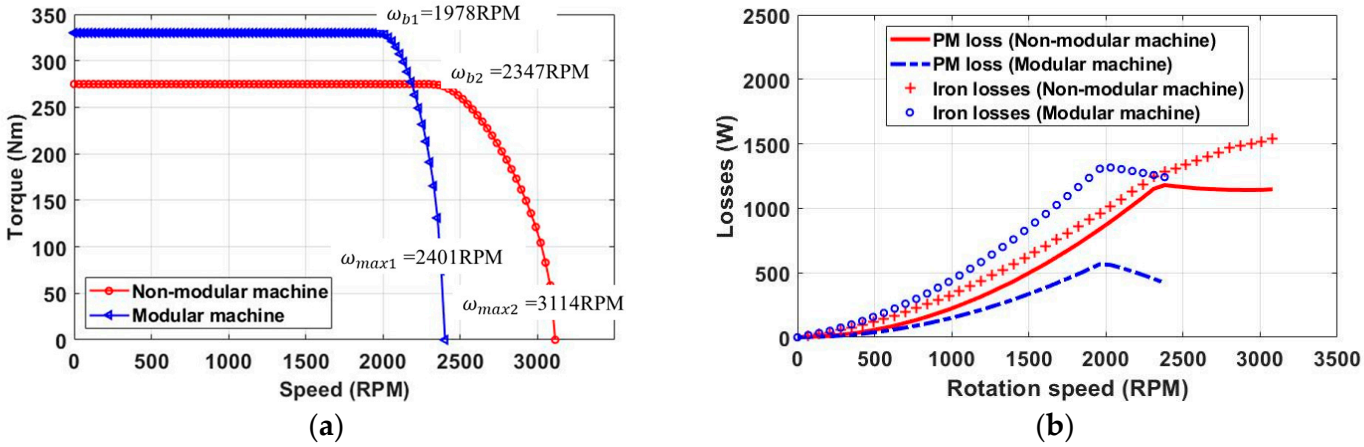

Figure 3. (**a**) Torque and (**b**) losses vs. speed for the modular and non-modular machines.

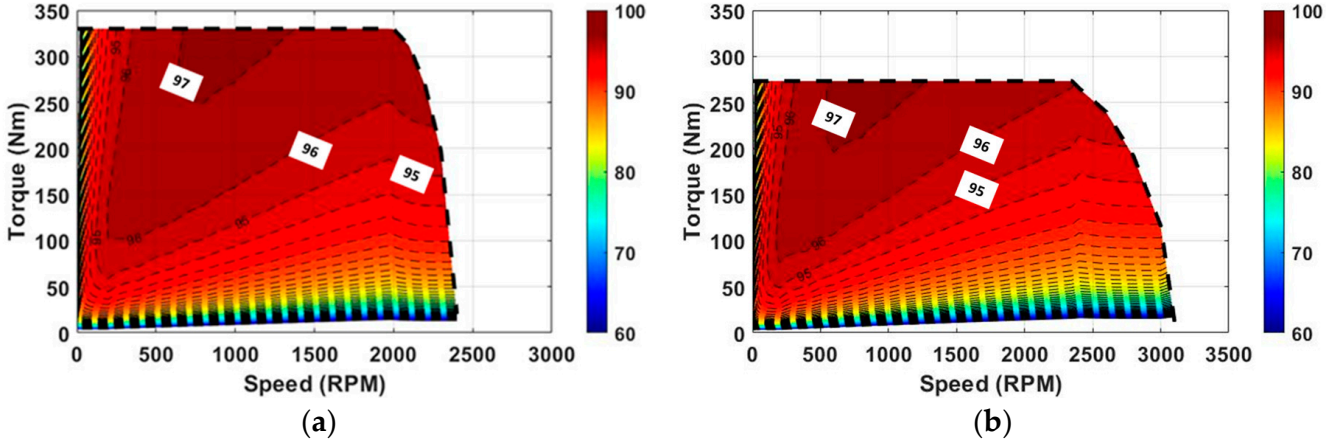

Figure 4. Efficiency maps of (**a**) modular machine and (**b**) non-modular machine.

2. Demagnetization Analysis

2.1. Mechanism of Magnet Irreversible Demagnetization

The temperature-dependent B(H) curves for the magnet material (N35H) used in this paper are shown in Figure 5a. It is found that, with temperature rise, the remanence is reduced, which can reduce the magnet MMF and the machine EM performance. In addition, the temperature rise can also reduce the coercivity but increase the knee point, which leads to easier magnet irreversible demagnetization. This can be explained by Figure 5b. For a given operating temperature and under different load conditions, the working point moves following the original demagnetization curve having a remanence B_{r0}. Since the working points have the same B_{r0}, the demagnetization will be reversible. However, if the working point moves

to below the knee point, it will follow a new demagnetization curve with a lower remanence (B_{r1}). This permanent loss of magnetization is so called "irreversible demagnetization". After the irreversible demagnetization, the machine will operate under the new B(H) curve with reduced remanence but with the same slope as the original B(H) curve [16,17].

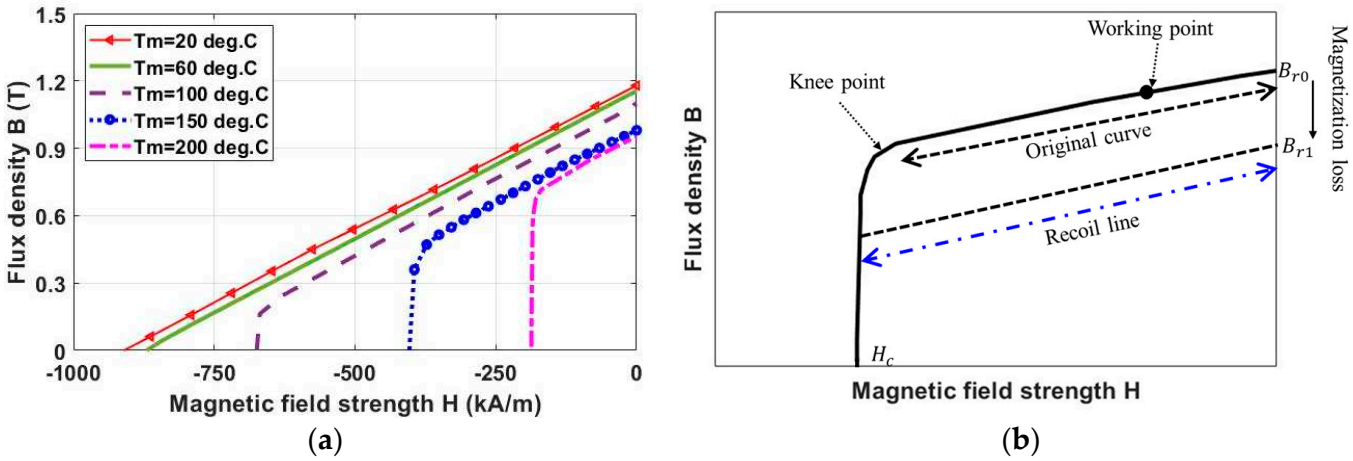

Figure 5. B(H) curves of the used PM material. (**a**) Temperature-dependent B(H) curves and (**b**) reversible and irreversible demagnetizations.

2.2. Demagnetization without EM-Thermal Coupling

The magnet flux density is essential for investigating the machine demagnetization characteristics and evaluating the machine demagnetization withstand capability. This is because, under the same operating condition, the machine with higher magnet flux density will generally have better demagnetization withstand capability. It is known that magnet flux density (B_m) depends on the reluctance of the magnetic circuit (R), the magnetomotive force (MMF) generated by PMs (F_m) and armature current (F_c), and can be calculated by:

$$\begin{cases} \Phi = \dfrac{F_M + F_c}{R} \\ B_m = \dfrac{\Phi}{A} \end{cases} \tag{1}$$

where Φ and A are the flux in the magnet and magnet area, respectively.

F_m and F_c can be described by:

$$\begin{cases} F_m = \dfrac{B_r L_{mag}}{\mu_0 \mu_r} \\ F_c = Ni \end{cases} \tag{2}$$

where B_r, μ_0, μ_r, L_{mag}, N, and i are the magnet remanence, vacuum permeability, magnet relative permeability, magnet thickness, number of turns and magnitude of armature current. It is worth noting that the magnet properties, e.g., remanence (B_r) and coercivity (H_c), are temperature-dependent as described by [18]:

$$\begin{cases} B_r(T) = B_r(T_0)\left[1 + \alpha_1(T - T_0) + \alpha_2(T - T_0)^2\right] \\ H_c(T) = H_c(T_0)\left[1 + \beta_1(T - T_0) + \beta_2(T - T_0)^2\right] \end{cases} \tag{3}$$

where T_0 is the reference temperature and α_1, α_2, β_1 and β_2 are temperature-dependent coefficients. α_1, α_2, β_1 and β_2 for the chosen magnet material in this paper are -1.2×10^{-3}, -1.5×10^{-9}, -6.9×10^{-3} and 1.17×10^{-5}, respectively.

According to Equations (1)–(3), the magnet flux density variation can be contributed from three sources:

1. PM field only: the MMF generated by PMs (F_m) can demagnetize the magnets.
2. Armature field only: the MMF generated by 3-phase armature currents (F_c), particularly under flux weakening operation or during short-circuit fault, can lead to magnet demagnetization.
3. Temperature rise: as mentioned previously, the coercivity of most magnets (except for Ferrite) reduces while the knee point increases to be closer to the magnet working point, making the magnets prone to irreversible demagnetization.

In order to investigate the magnet demagnetization, the points along the center line within a PM (as shown in Figure 6) have been chosen. This is mainly due to the fact that the magnet in this region is more easily affected by demagnetization than other regions [5]. It is worth noting that, in order to separate the influence of the above three sources on the magnet demagnetization, a range of magnet temperatures will be used first in this section without adopting coupled EM-thermal modelling, which will be investigated in Section 2.2.4 for more accurate temperature prediction.

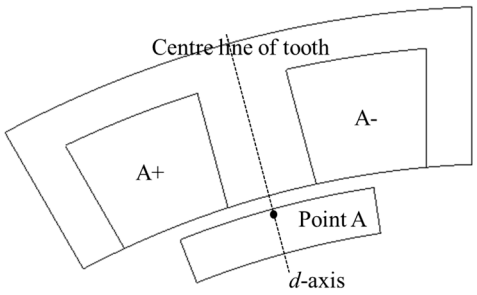

Figure 6. Points chosen for demagnetization analysis within the PM.

Without considering the magnet temperature variation, temperature rise in particular, the magnet demagnetization is mainly due to the MMFs produced by the PMs and armature currents, especially the negative d-axis current, as shown in Figure 7. It is found that, at a magnet operating temperature of 20 °C, when the load current is smaller than a critical value, e.g., 200 A for the modular machine and 300 A for the non-modular machine, the minimum flux density is almost constant when the d-axis current reduces. After the critical value, the minimum magnet flux density reduces almost linearly with reducing d-axis current. Compared with the non-modular machine, the modular machine is found to be able to improve the minimum magnet flux density at different load currents. This means that the introduced flux gaps can improve the demagnetization withstand capability.

The flux density versus rotor position for the modular and non-modular machines is also investigated, as shown in Figure 8. It is found that, if the current is smaller than the critical value, the minimum magnet flux density is reached when the center line of the PM is aligned with the center line of the slot (rotor position 2 in Figure 8). In addition, the values of the minimum flux density are almost the same for different currents. On the contrary, when the current is larger than the critical value, the minimum magnet flux density can be reached when the center line of the PM is aligned with the center line of the tooth (rotor position 1 in Figure 8). In addition, when the selected PM rotates to the flux gap region, the magnet flux density will reduce until the center line of the PM is aligned with the center line of the flux gap (rotor position 3 in Figure 8). This magnet flux density variation is caused by the combined influence between machine topology, MMFs generated by PMs, and armature currents, which will be detailed in the following sections.

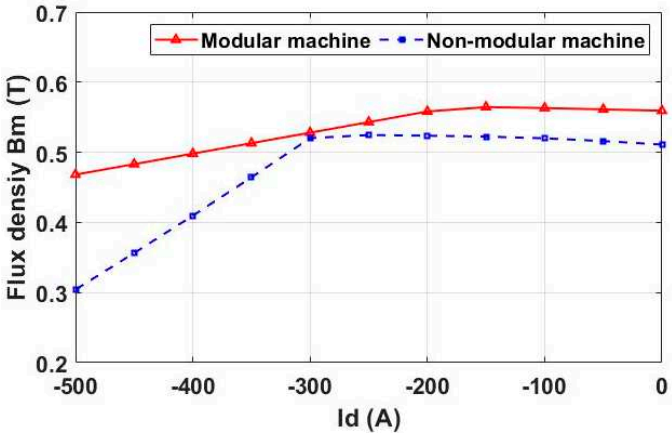

Figure 7. Minimum magnet flux density (radial component) at 20 °C at point A vs. the d-axis current for the investigated machines.

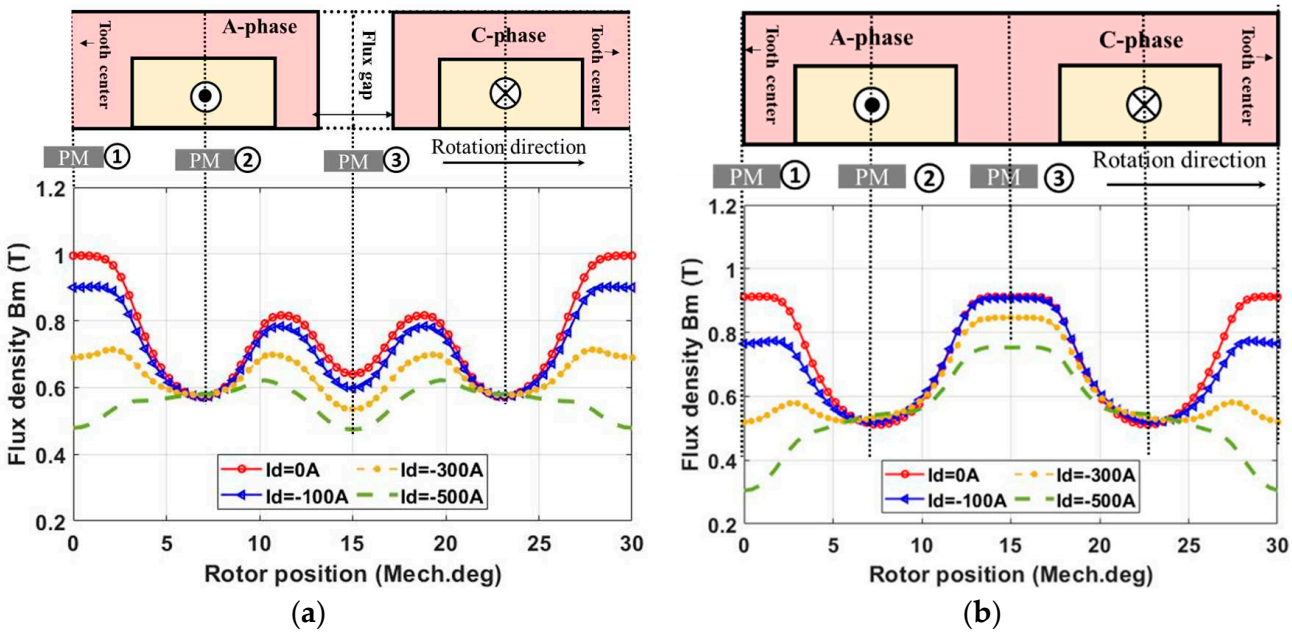

Figure 8. Magnet flux density (radial component) at 20 °C at point A for the (**a**) modular and (**b**) non-modular machines.

2.2.1. PM Field Only

In order to evaluate the influence of demagnetization caused by only the PM field while under the influence of negative d-axis current, the modular and non-modular machines have been simulated at a PM temperature of 20 °C. By adopting the FP method, the armature field has been removed and the magnet flux density variation due to the PM field for both investigated machines are shown in Figure 9. Without the armature field, the magnet flux density only depends on the reluctance of the magnetic circuit and the PM MMF (FM). It is found that, due to the non-linear characteristics of the iron core, reducing the d-axis current increase its relative permeability (μ_r); therefore, reduces the reluctance while increasing the magnet flux density. The variation in magnet flux density is significant for the non-modular machine as show in Figure 9b. However, it is found that, the flux density variation for the modular machine under different load currents is almost the same, as shown in Figure 9a. This means that, the introduced flux gaps in the modular machine can significantly reduce the PM flux density variation caused by the variation of iron core permeability.

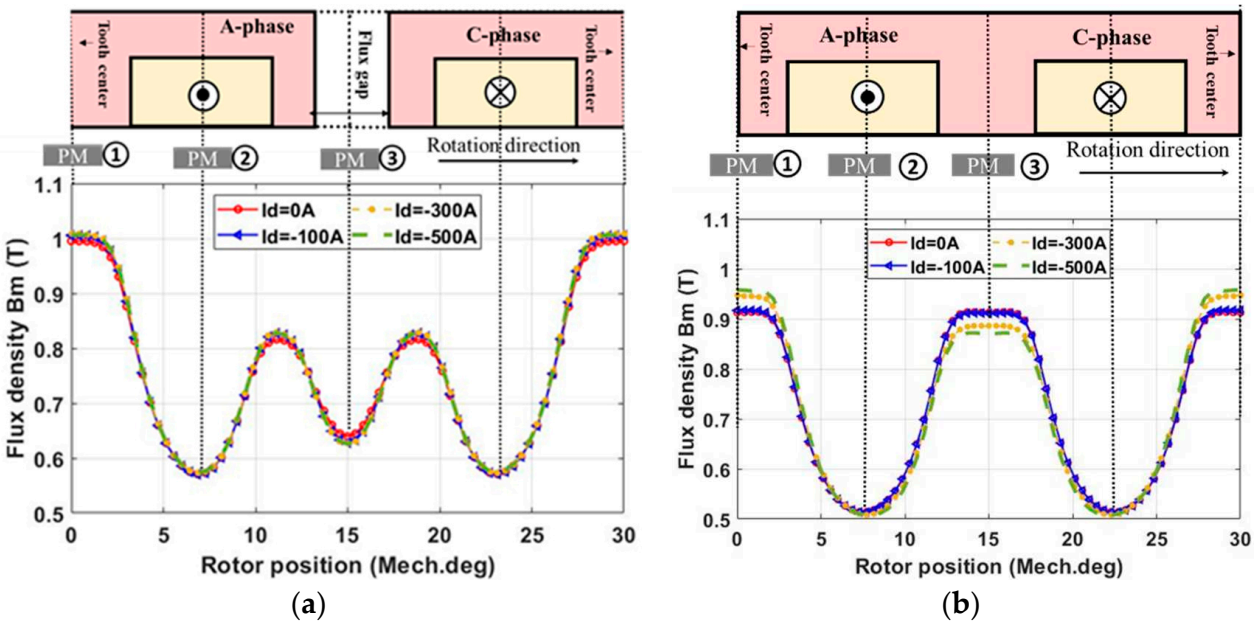

Figure 9. Magnet flux density (radial component) generated by PM source at point A within the selected PM vs. rotor position for the (**a**) modular and (**b**) non-modular machines.

For both the investigated machines, the maximum flux density is reached at the initial rotor position, i.e., the center line of the magnet is aligned with the center line of the tooth (rotor position 1 in Figure 9a). This is because the effective airgap length, and therefore the reluctance, are minimum when the rotor is at position 1. When the rotor rotates and the selected magnet is facing the slot opening, the reluctance increases because of the small relative permeability of the copper wires (μ_r = 1) in the stator slot. Therefore, the magnet flux density reduces and reaches its minimum value when the center line of the magnet is aligned with the center line of the slot opening (rotor position 2 in Figure 9a). The introduced flux gaps have the same effect as the slot openings, which also reduce the magnet flux density when the selected magnet rotates to the flux gap region. The magnet flux density will keep reducing until the center line of the magnet is aligned with the center line of the flux gap (rotor position 3 as shown in Figure 9a).

The results above are for a single flux gap width (10 mm), the minimum magnet flux density variation against the flux gap width has also been investigated, as shown in Figure 10a. It is found that, when the flux gap width is smaller than 13 mm, an increasing flux gap width leads to increased minimum flux density. This means improved magnet demagnetization withstand capability. The reason is that, increasing flux gap width leads to reduced slot opening, and hence, a reduced effective airgap length at rotor position 2. As a result, the minimum flux density at position 2 will be increased, as shown by the red curve in Figure 10b. However, when the flux gap width is larger than a critical value (13 mm for the investigated modular machine in this paper), the minimum magnet flux density reduces with increased flux gap width. This is because the flux gap has the same effect with the slot openings. If the flux gap width is large enough (13 mm for the investigated modular machine), the magnet flux density at rotor position 3 will be smaller than that at rotor position 2 due to the larger effective airgap length, as shown by the blue curve in Figure 10b. This means that an optimal flux gap width (13 mm) can be found from the magnet demagnetization withstand capability point of view.

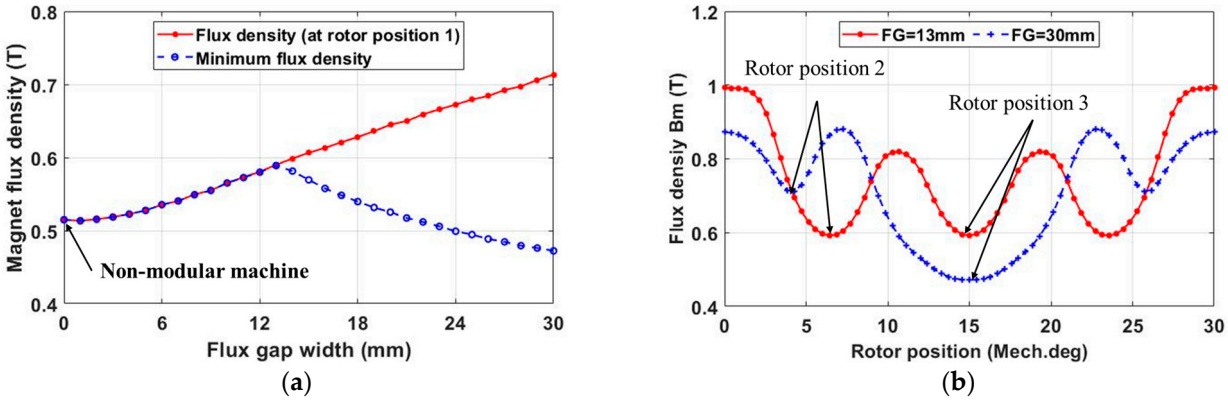

Figure 10. Magnet flux density (radial component) at point A generated by PM MMF at 20 °C for the modular machine. (**a**) Minimum magnet flux density vs. flux gap width and (**b**) magnet flux density vs. rotor position while the flux gap widths are 13 mm and 30 mm.

2.2.2. Armature Field Only

Apart from the PM field in the previous section, the applied armature currents can also generate demagnetizing MMF. Again, using the FP method, the magnet flux density (at point A) due to only the armature field against the load current has been calculated, as shown in Figure 11. The magnet flux density now depends on the load current, and the effective airgap length, as described by Equations (1) and (2). As a result, for both the modular and non-modular machines, at the initial rotor position 1 where the d-axis is aligned with the center line of the tooth of the A-phase, the magnitude of the A-phase current reaches its maximum value, and the effective airgap length is the smallest. This leads to the most significant demagnetization, and hence, the minimum magnet flux density. When the rotor rotates towards the slot opening, the effective airgap length is increased. Together with a reduced A-phase current, the magnet flux density generated by the applied armature field at point A is increased. However, when the rotor rotates by 90 electrical degrees, i.e., $45/7 \approx 6.4$ mechanical degrees, named as rotor position 4 in this paper, the A-phase current is 0 A, while the B-phase current is equal to minus C-phase current. Hence, the magnet flux density at point A is 0 T.

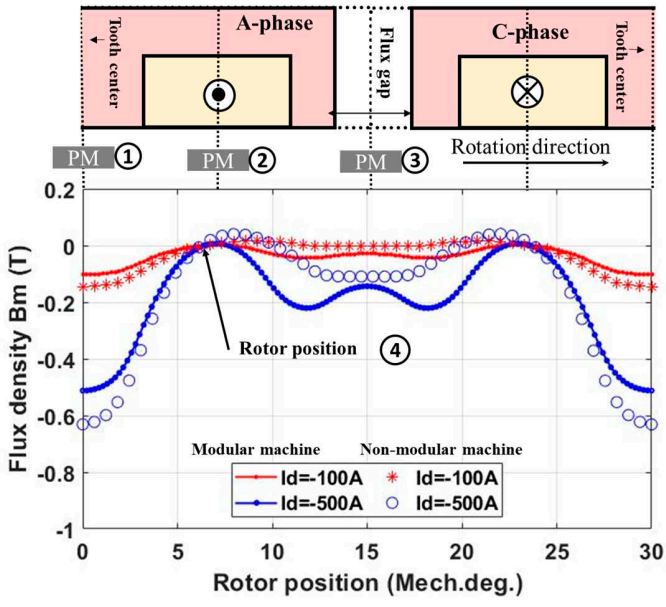

Figure 11. The magnet flux density (radial component) at point A generated by an applied 3-phase armature current at 20 °C for the modular machine with different load currents.

According to Equation (2), the armature MMF is proportional to the current amplitude. Therefore, when the current amplitude increases, the minimum magnet flux density reduces, as shown in Figure 12a. This is true for both the modular and non-modular machines. However, the modular machine is able to increase the minimum magnet flux density, which results from the increased effective airgap length due to the introduced flux gaps as mentioned in the previous section. However, this increase in magnet flux density is insignificant when the flux gap width is larger than 10 mm, as shown in Figure 12b. In addition, the improved minimum magnet flux density for the modular machine reveals that the demagnetization caused by armature MMF in the modular machine can also be mitigated by the introduced flux gaps. This is similar to the demagnetization caused by the PM MMF in previous section.

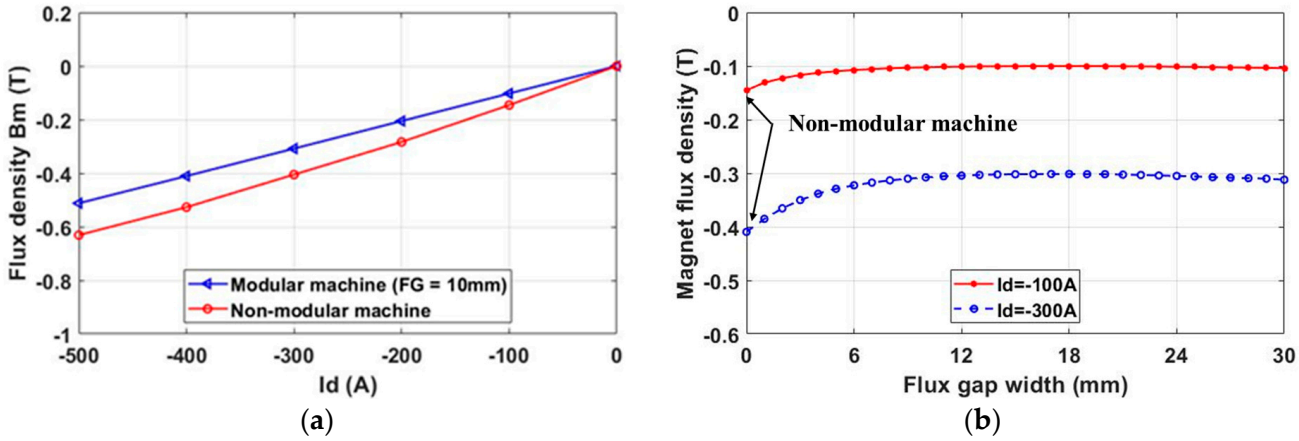

Figure 12. The minimum magnet flux density at point A generated by applied 3-phase armature currents at 20 °C. (**a**) B_m vs. current amplitude, and (**b**) B_m vs. FG width for I_d = −100 A and −300 A.

2.2.3. Demagnetization with Temperature Rise

As mentioned previously, apart from the influence of the MMFs produced by the magnets and armature currents, the temperature rise can also lead to further magnet demagnetization. To evaluate the magnet demagnetization due to temperature rise, the minimum magnet flux density at point A versus magnet temperature and d-axis current are shown in Figure 13. For both the modular and non-modular machines, increasing the armature field leads to reduced minimum magnet flux density. In addition, when the PM temperature is below 150 °C, the demagnetization is insignificant and the reduction in minimum magnet flux density is small. However, when the magnet temperature increases to beyond 150 °C, the machine demagnetization withstand capability significantly deteriorates. As a result, this dramatically reduces the magnet flux density. The overheating of the magnets can even lead to a change in magnet polarity, as shown in Figure 13.

Compared with the non-modular machine, the modular machine (as shown in Figure 13) has higher magnet flux density at different magnet temperatures and d-axis currents. This means that the introduced flux gaps are able to improve the demagnetization withstand capability at different operating conditions.

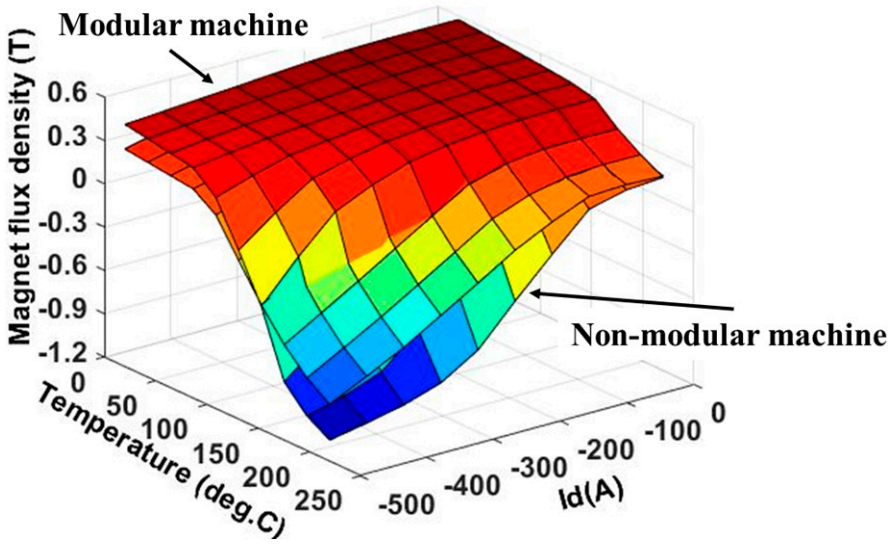

Figure 13. The minimum magnet flux density (radial component) at point A for the investigated machines under different operating conditions.

2.2.4. Demagnetization with Coupled EM-Thermal Modelling

As discussed in previous sections, it is found that the machine topologies, load current and temperature rise can significantly affect the flux density distribution within PMs. This will, in turn, affect the losses, e.g., stator and rotor iron core losses, PM eddy current loss, and EM torque. Together with the increase in copper loss due to the temperature-dependent electrical resistivity of copper [the coefficient is $3.69 \times 10^{-3}/°C$ [13] (p. 76), the variation of losses caused by demagnetization will also lead to machine temperature variation, which will again affect the EM's performance. Therefore, the coupled EM-thermal modelling, as described by the flowchart shown in Figure 2, is essential to account for the interaction between the EM and thermal performance. In this section, the coupled EM-thermal modelling is implemented for both investigated machines. Three operating conditions are considered for the investigations, e.g., condition 1 (rated current $I_d = 0$ A and $I_q = 100$ A), condition 2 (flux weakening $-$ $I_d = I_q = 50\sqrt{2}$ A), and condition 3 (3 times the rated current $I_d = 0$ A and $I_q = 300$ A).

Some assumptions need to be made for the coupled EM-thermal modelling such as:

1. The electrical resistivity of the PM and iron core are independent of the temperature rise. This is because the increase in resistivity of the PM and iron core are negligible when the temperature rise is lower than 300 °C [19].
2. For different operating conditions, only steady-state performance is considered to simplify the analyses.
3. In order to avoid the change of magnet polarity, as shown in Figure 13, the investigated machines are assumed to operate less than 30 min when they are operated under three times the rated current.

It is worth noting that the coupled EM-thermal model is quite computationally intensive. Therefore, instead of using a 3D finite element (FE) thermal or 3D computational fluid dynamics (CFD) model, 3D lumped parameter thermal network (LPTN) models for both the modular and non-modular machines have been developed based on the models in Motor-CAD. Different from the non-modular machine, the LPTN of the modular machine should include extra equivalent thermal resistances to represent the heat convection at the flux gap surfaces. The stator segments with heat convection are shown in Figure 14a, and the heat conduction in the stator is shown in Figure 14b. The rotor thermal network is not shown as it is the same as that of the non-modular machine. The equivalent thermal resistance of the segmental stators and new topologies of the windings for the modular machines should be re-calculated. For example, the segmental stator back-iron and active

winding will be considered as cylindrical components with angular spans α as shown in Figure 15a, and its equivalent thermal network is shown in Figure 15b. The equivalent thermal resistances are derived by [20]:

$$R_{1r} = \frac{1}{2\alpha\lambda L}\left[1 - \frac{2r_2^2 \ln\left(\frac{r_1}{r_2}\right)}{(r_1^2 - r_2^2)}\right] \tag{4}$$

$$R_{2r} = \frac{1}{2\alpha\lambda L}\left[\frac{2r_1^2 \ln\left(\frac{r_1}{r_2}\right)}{(r_1^2 - r_2^2)} - 1\right] \tag{5}$$

$$R_{1a} = R_{2a} = \frac{L}{\alpha\lambda(r_1^2 - r_2^2)} \tag{6}$$

$$R_{3r} = \frac{-1}{4\alpha\lambda L(r_1^2 - r_2^2)}\left[\left(r_1^2 + r_2^2\right) - \frac{4r_2^2 \ln\left(\frac{r_1}{r_2}\right)}{(r_1^2 - r_2^2)}\right] \tag{7}$$

$$R_{3a} = \frac{-L}{3\alpha\lambda(r_1^2 - r_2^2)} \tag{8}$$

where r_1, r_2 and L are the radius of the outer surface, radius of the inner surface, and stack length, respectively. It is worth noting that, if the components are without heat generation, resistance R_{3r} and R_{3a} is equal to 0. The equivalent thermal resistance of the heat convection at flux gap surfaces is also derived by:

$$R_h = \frac{1}{hS_h} \tag{9}$$

where h is the convection coefficient at the flux gap surfaces, which are calculated by CFD.

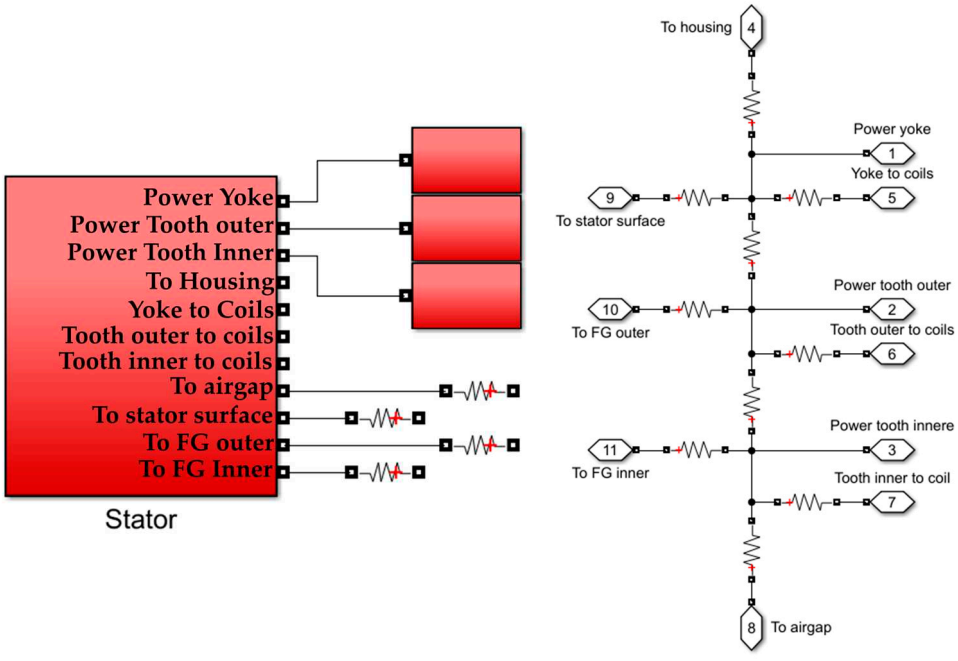

(**a**) (**b**)

Figure 14. The 3D LPTN model for the stator for the modular machine. (**a**) Heat convection block. (**b**) Heat conduction block. FG is the flux gap.

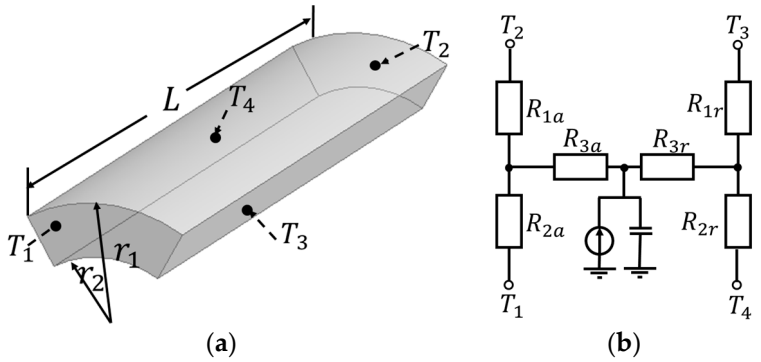

(**a**) (**b**)

Figure 15. (**a**) Cylindrical components in electrical machines with angular spans α and (**b**) its equivalent thermal network. T_1, T_2, T_3 and T_4 are the temperatures of the front, rear, outer and inner surfaces, respectively.

Using the coupled EM-thermal model, the average PM and coil temperatures for both investigated machines have been obtained, as shown in Table 3. Due to the magnet's temperature rise, the magnet flux density is reduced for both the investigated machines under different operating conditions, as shown in Figure 16. In addition, the magnet flux density in condition 2 is slightly smaller than that in condition 1. This reduction is mainly due to the introduced d-axis current for flux weakening. However, the amplitude of the d-axis current in condition 2 is relatively small, and therefore, the demagnetization caused by the armature field is only marginal.

Table 3. Average steady state of the PM and coil temperatures.

	Modular Machine		Non-Modular Machine	
	Tm (°C)	Tc (°C)	Tm (°C)	Tc (°C)
Condition 1	160	151	158	142
Condition 2	153	146	148	148
Condition 3	150	152	140	129

Note: Tm and Tc are the average temperatures of the magnets and coils, respectively.

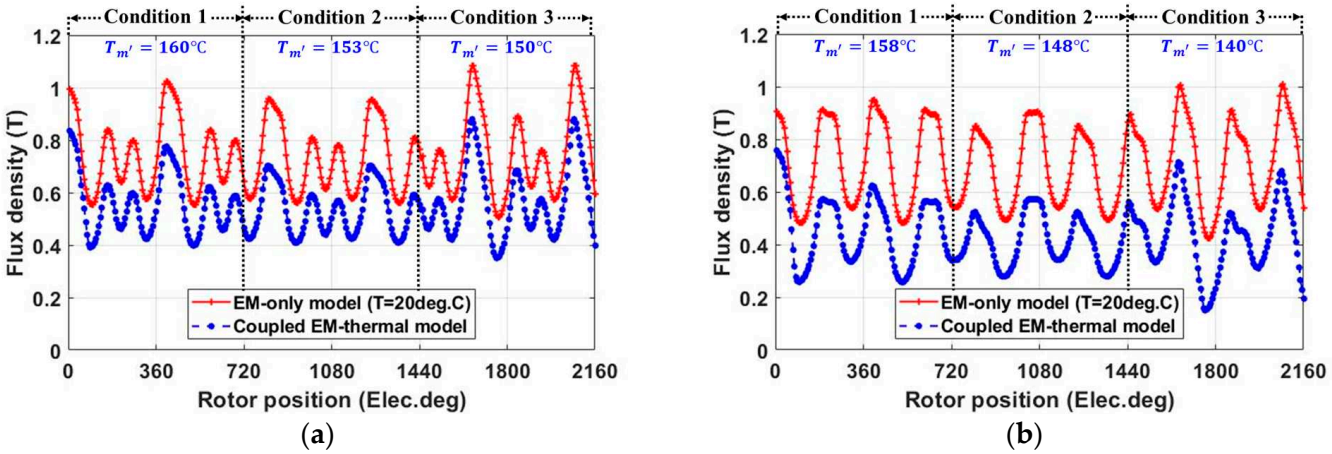

(**a**) (**b**)

Figure 16. Magnet flux density variation under different operating conditions calculated for (**a**) modular and (**b**) non-modular machines. $T_{m'}$ denotes the average magnet temperature.

It is worth noting that the PM eddy current loss is proportional to the magnet flux density variation rate (dB_b/dt). Compared with the non-modular machine, the magnet flux density variation rate of the modular machine is smaller, as shown in Figure 16. This is because the increase in the effective airgap length, caused by the introduced flux gaps, can

reduce the magnet flux density variation rate, and hence, can reduce the PM eddy current loss, as shown in Figure 17. This decrease can be more significant when the machines operate under overload conditions, e.g., three times the rated current.

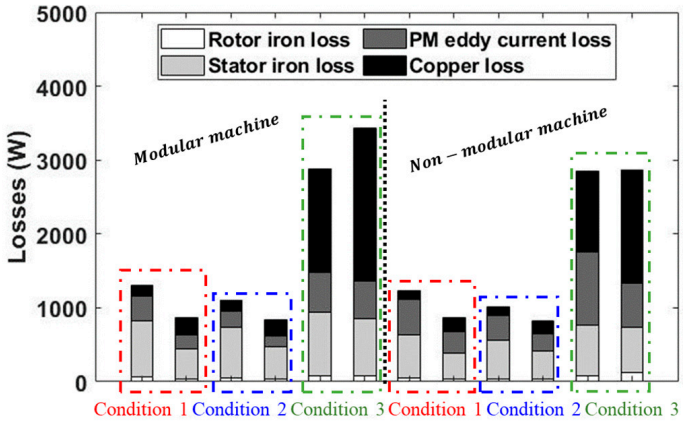

Figure 17. Losses (including stator and rotor iron losses, and PM eddy current loss) of both investigated machines under different operating conditions. For each load condition, the left-hand bar reflects the losses obtained by using the EM-only model and the right-hand bar reflects the losses obtained by using the EM-thermal coupled model.

In addition, with the coupled EM-thermal model, the losses for different load conditions, including the PM eddy current loss, and stator and rotor iron core losses, are all reduced for both of the investigated machines. This is also due to the demagnetization caused by the PM's temperature rise. Furthermore, due to higher copper loss resulting from the reduced slot area, the temperatures within the modular machine are higher than those within the non-modular machine under a peak phase current of 100 A (conditions 1 and 2). For example, with the introduced flux gaps, the PM temperature increases from 158 °C and 148 °C to 160 °C and 153 °C for the conditions 1 and 2, respectively. When the machines operate the condition 3, e.g., I_q = 300 A, the advantage of flux gaps in reducing the PM eddy current loss is more evident, as shown in Figure 17. However, the increase in copper loss can also be more significant due to increased load current. This results in a higher coil temperature, which can further increase the copper loss. As a result, the modular machine has a higher copper loss and coil temperature (increase from 129 °C (non-modular) to 152 °C (modular)). In addition, the PM temperature of the modular machine is also affected by this high copper loss, increasing from 140 °C (non-modular) to 150 °C (modular). However, it is worth noting that these results are obtained under the condition that the number of turns per phase and the phase current are the same between the modular and non-modular machines. Given the fact that the modular machine can achieve higher average torque, then, if under the same average torque conditions, the copper loss of the modular machine will be smaller than that of the non-modular counterpart [4]. This will lead to lower coil and PM temperatures within the modular machine.

With the coupled EM-thermal modelling, the partial irreversible demagnetization has also been investigated for both the modular and non-modular machines. The irreversibly demagnetized areas (colored), where the remanence is reduced, are shown in Figure 18. It is found that both machines will experience irreversible demagnetization, but the modular machine has a smaller irreversible demagnetization region than the non-modular machine. This means that the introduced flux gaps can improve the demagnetization withstand capability under different load conditions.

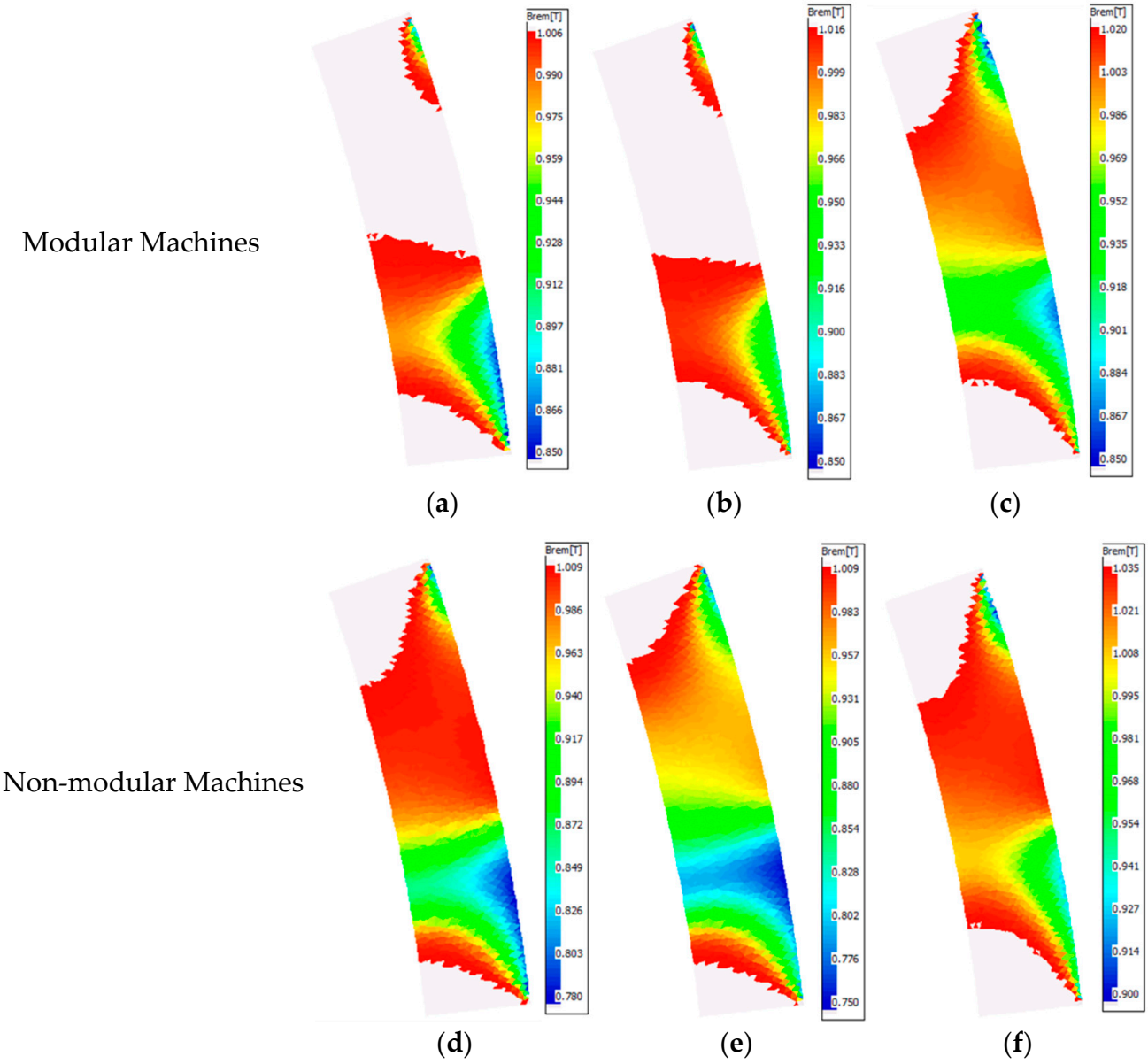

Figure 18. Remanence distribution of the PM obtained using the coupled EM-thermal model of Motor-CAD for (**a**) condition 1, $T_{m'}$ = 160 °C; (**b**) condition 2, $T_{m'}$ = 153 °C; (**c**) condition 3, $T_{m'}$ = 150 °C; (**d**) condition 1, $T_{m'}$ = 158 °C; (**e**) condition 2, $T_{m'}$ = 148 °C; and (**f**) condition 3, $T_{m'}$ = 140 °C.

Torque, as one of the most important EM performances for the machines, is also affected by the demagnetization. Compared with the EM-only modelling, the torque of the modular and non-modular machine calculated by using the coupled EM-thermal modelling is lower. This is mainly due to the demagnetization caused by the PM temperature rise, as shown in Figure 19. Even though the modular machine has higher PM temperature due to copper loss, the decrease in torque is less significant than the non-modular machine. It is shown that, the improved demagnetization withstand capability and reduced PM eddy current loss due to flux gaps allow the modular machines to have better EM performance.

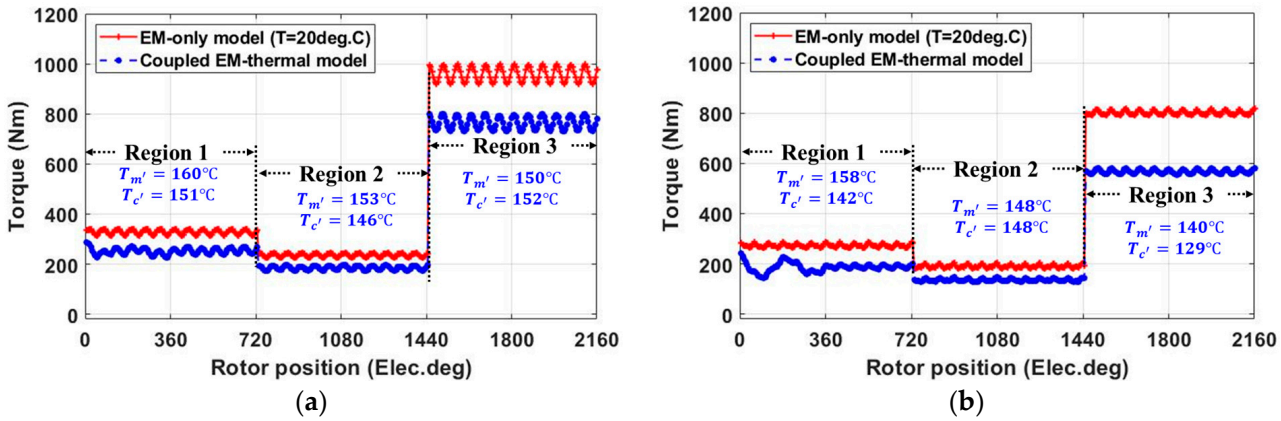

Figure 19. On-load torque vs. rotor position for (**a**) modular and (**b**) non-modular machines with and without considering EM-thermal coupling. $T_{m'}$ and $T_{c'}$ denote the average steady state magnet and coil temperatures obtained by the coupled EM-thermal model.

3. Conclusions

In this paper, the demagnetization caused by the PM field, applied armature field and magnet temperature rise has been investigated for both modular and non-modular machines by adopting a coupled EM-thermal modelling. When temperature varies, the temperature-dependent material properties, e.g., the magnet remanence and coercivity and copper resistivity, will also change, leading to different losses including stator and rotor core iron losses, magnet eddy current loss and copper loss. The changed losses will, in turn, lead to temperature variation within electrical machines. Therefore, it is essential to adopt the coupled EM-thermal modelling in order to more accurately predict the machine EM and thermal performances.

By employing the coupled EM-thermal models, the magnet flux density variation, magnet eddy current loss, and irreversible magnet demagnetization have been compared between modular and non-modular machines. It is found that, the introduced flux gaps in the modular machine are able to improve the machine demagnetization withstand capability. In addition, they can also reduce the PM eddy current loss. Compared to the non-modular machine, the improved demagnetization withstand capability of the modular machine leads to a smaller irreversible demagnetization region and also significantly improves on-load torque. Benefits from this higher demagnetization capability, such as the improved EM performance for the modular machine, can be more significant with the coupled EM-thermal modelling, as listed in Table 4. Compared with non-coupled modelling (listed in Table 2), the efficiency of the modular machine is improved by 0.2%, while it is reduced by 1.2% for the non-modular machine.

Table 4. EM performance with coupled models for the modular and non-modular SPM machines.

	Torque (Nm)	Power (kW)	Efficiency (%)
Modular machine	326	51.2	97.1
Non-modular machine	270	42.4	95.6

Author Contributions: Writing—original draft, W.Z.; Writing—review & editing, G.-J.L. and Z.-Q.Z.; Funding acquisition, B.R., Y.C.C. and M.M. All authors have read and agreed to the published version of the manuscript.

Funding: This project is partially funded by Motor Design Limited.

Data Availability Statement: Not applicable.

Conflicts of Interest: The authors declare no conflict of interest.

References

1. Spooner, E.; Williamson, A.; Catto, G. Modular design of permanent-magnet generators for wind turbines. *IEE Proc.-Electr. Power Appl.* **1996**, *143*, 388–395. [CrossRef]
2. Akita, H.; Nakahara, Y.; Miyake, N.; Oikawa, T. New core structure and manufacturing method for high efficiency of permanent magnet motors. In Proceedings of the 38th IAS Annual Meeting on Conference Record of the Industry Applications Conference, Salt Lake City, UT, USA, 12–16 October 2003; pp. 367–372.
3. Zhang, W.; Li, G.; Zhu, Z.; Ren, B.; Michon, M. Optimization of Modular SPM Machines Considering Stator Modularity. In Proceedings of the 2021 IEEE International Electric Machines & Drives Conference (IEMDC), Hartford, CT, USA, 17–20 May 2021; pp. 1–6.
4. Li, G.; Zhu, Z.; Chu, W.; Foster, M.; Stone, D. Influence of flux gaps on electromagnetic performance of novel modular PM machines. *IEEE Trans. Energy Convers.* **2014**, *29*, 716–726. [CrossRef]
5. Li, G.; Ren, B.; Zhu, Z.; Foster, M.; Stone, D. Demagnetization withstand capability enhancement of surface mounted PM machines using stator modularity. *IEEE Trans. Ind. Appl.* **2017**, *54*, 1302–1311. [CrossRef]
6. Lyu, S.; Yang, H.; Lin, H.; Zhu, Z.; Zheng, H.; Pan, Z. Influence of design parameters on on-load demagnetization characteristics of switched flux hybrid magnet memory machine. *IEEE Trans. Magn.* **2019**, *55*, 1–5. [CrossRef]
7. McFarland, J.D.; Jahns, T.M. Investigation of the rotor demagnetization characteristics of interior PM synchronous machines during fault conditions. *IEEE Trans. Ind. Appl.* **2013**, *50*, 2768–2775. [CrossRef]
8. Choi, G.; Jahns, T. Interior permanent magnet synchronous machine rotor demagnetization characteristics under fault conditions. In Proceedings of the 2013 IEEE Energy Conversion Congress and Exposition, Denver, CO, USA, 15–19 September 2013; pp. 2500–2507.
9. McFarland, J.D.; Jahns, T.M.; El-Refaie, A.M. Demagnetization performance characteristics of flux switching permanent magnet machines. In Proceedings of the 2014 International Conference on Electrical Machines (ICEM), Berlin, Germany, 2–5 September 2014; pp. 2001–2007.
10. Li, G.J.; Taras, P.; Zhu, Z.Q.; Ojeda, J.; Gabsi, M. Investigation of irreversible demagnetisation in switched flux permanent magnet machines under short–circuit conditions. *IET Electr. Power Appl.* **2017**, *11*, 595–602. [CrossRef]
11. Kim, H.-K.; Hur, J. Dynamic characteristic analysis of irreversible demagnetization in SPM-and IPM-type BLDC motors. *IEEE Trans. Ind. Appl.* **2016**, *53*, 982–990. [CrossRef]
12. Sebastian, T. Temperature effects on torque production and efficiency of PM motors using NdFeB magnets. *IEEE Trans. Ind. Appl.* **1995**, *31*, 353–357. [CrossRef]
13. Dellinger, J.H. *The Temperature Coefficient of Resistance of Copper*; US Government Printing Office: Washington, DC, USA, 1911.
14. Taras, P.; Li, G.-J.; Zhu, Z.-Q.; Foster, M.P.; Stone, D.A. Combined multiphysics model of switched flux PM machines under fault operations. *IEEE Trans. Ind. Electron.* **2018**, *66*, 6737–6745. [CrossRef]
15. Shi, Y.; Wang, J.; Wang, B. Electromagnetic-thermal coupled simulation under various fault conditions of a triple redundant 9-phase PMASynRM. *IEEE Trans. Ind. Appl.* **2019**, *56*, 128–137. [CrossRef]
16. Woo, D.-K.; Jeong, B.H. Irreversible demagnetization of permanent magnet in a surface-mounted permanent magnet motor with overhang structure. *IEEE Trans. Magn.* **2015**, *52*, 1–6. [CrossRef]
17. Zhu, Z.; Pang, Y.; Howe, D.; Iwasaki, S.; Deodhar, R.; Pride, A. Analysis of electromagnetic performance of flux-switching permanent-magnet machines by nonlinear adaptive lumped parameter magnetic circuit model. *IEEE Trans. Magn.* **2005**, *41*, 4277–4287. [CrossRef]
18. Zhou, P.; Lin, D.; Xiao, Y.; Lambert, N.; Rahman, M. Temperature-dependent demagnetization model of permanent magnets for finite element analysis. *IEEE Trans. Magn.* **2012**, *48*, 1031–1034. [CrossRef]
19. Wu, K.; Yao, Y.; Klik, I. Electrical and magnetic properties of NdFeB films. *Appl. Surf. Sci.* **1997**, *113*, 174–177. [CrossRef]
20. Mezani, S.; Takorabet, N.; Laporte, B. A combined electromagnetic and thermal analysis of induction motors. *IEEE Trans. Magn.* **2005**, *41*, 1572–1575. [CrossRef]